

## **Effect of cobalt promotion on hydrotalcite-derived nickel catalyst for CO<sub>2</sub> methanation**

Paulina Summa\*<sup>1,2</sup>, Katarzyna Świrk<sup>3</sup>, Ye Wang<sup>4</sup>, Bogdan Samojeden<sup>1</sup>, Magnus Rønning<sup>3</sup>, Changwei Hu<sup>4,5</sup>, Monika Motak<sup>1</sup>, Patrick Da Costa<sup>2</sup>

<sup>1</sup>AGH University of Science and Technology, Faculty of Energy and Fuels, Poland

<sup>2</sup>Institut Jean le Rond d'Alembert, Sorbonne Université, CNRS UMR 7190, 2 place de la gare de ceinture, Saint Cyr L'Ecole, France

<sup>3</sup>Department of Chemical Engineering, Norwegian University of Science and Technology (NTNU), Trondheim, Norway

<sup>4</sup>College of Chemical Engineering, Sichuan University, P. R. China

<sup>5</sup>Key Laboratory of Green Chemistry and Technology, Ministry of Education, College of Chemistry, Sichuan University, P. R. China

\*summa@agh.edu.pl, patrick.da\_costa@sorbonne-universite.fr

### **Abstract:**

A series of cobalt-promoted Ni-Mg-Al hydrotalcite-derived catalysts were tested towards CO<sub>2</sub> methanation reaction. The best among examined catalysts was the one with 1 wt% of cobalt in fresh hydrotalcite, obtaining 77% of CO<sub>2</sub> conversion and 99% of CH<sub>4</sub> selectivity at 300 °C. Above that temperature, the catalyst was working with-near-equilibrium parameters. It was also stable for up to 24 hours on stream. Other cobalt-containing samples were likewise very active and selective during the time on stream. Due to the use of a low amount of cobalt (0.5-4 wt%) the Co-Ni alloy was not the subject of research – both materials formed probably solid solution of cobalt in the nickel matrix. Although the behavior of cobalt as a textural and electronic promoter was confirmed. Co was found to improve reducibility of nickel species, hydrogen uptake, and the acidic/basic properties by increasing the number of medium strength and strong basic sites. Tendency to sintering of nickel crystallites on cobalt-promoted catalysts was not confirmed in this study, however, with increased content of Co, bigger metal crystallites were formed under the reduction conditions.

Keywords: Mixed oxides, Nickel, Co-promotion, Methanation, Basicity

## 1. Introduction

The emission of CO<sub>2</sub> to the atmosphere is constantly increasing since the industrial revolution. Though before the XIX century, its concentration in the atmosphere varied, the medium value was estimated to be ca. 280 ppm [1,2]. Since then, the CO<sub>2</sub> level has been constantly increasing. The current concentration is ca. 410 ppm [3]. However, some of the forecasts expect it to double before the end of the XXI century [4,5]. Even though CO<sub>2</sub> is a crucial molecule for the Earth's ecosystem, the abundance in the atmosphere is related to long-term negative environmental effects [6].

Several catalytic processes are commercially used to utilize CO<sub>2</sub>, e. g. production of cyclic carbonates, dimethyl carbonate, and CO<sub>2</sub> hydrogenation to methanol [7]. Furthermore, CO<sub>2</sub> methanation which is an emerging process as well, is nowadays developed by Audi, DVGW, and other companies [8]. Catalysts for methanation were extensively investigated in order to find a better alternative to the currently applied Ni/Al<sub>2</sub>O<sub>3</sub> [9]. Nickel-based catalysts are a satisfactory compromise between costs and activity in the methanation process. However, these catalysts are not stable during time on stream (TOS). The two main deactivation causes are sintering of the Ni active phase and the carbon deposition during TOS[10]. The presence of water vapor and hot-spots formation support agglomeration of active sites, which directly reduces the dispersion of nickel and surface free energy [11]. Coke formation resulting in carbonate and formate species is a reversible setback – deposit is easily gasified either with hydrogen or water vapor. Stable carbon species such as filaments, fibers, and whiskers are irreversibly deactivating the catalysts [12,13].

A variety of materials have been tested as CO<sub>2</sub> methanation catalysts. Among them, the most promising results were obtained with noble metal-based catalysts, but due to high cost and limited availability, a more economical and accessible solution is necessary. The activity of metallic centers for the methanation reaction is assumed to be correlated as follows:

Ru>Ir>Rh>Ni>Co>Os>Pt>Fe>Mo>Pd>Ag [14]. Additionally, the choice of a proper support can modify the properties of the catalyst. Silica-based supports such as mesostructured silica nanoparticles (MSN), MCM-41, and SiO<sub>2</sub> were investigated, among which MSN gave the most promising results. It may be attributed to a high concentration of basic sites and the presence of intra- and inter-particle porosity [15,16]. ZrO<sub>2</sub> is interesting support due to CO<sub>2</sub>/CO adsorption capability and optimal acidic/basic properties. In the monoclinic form, ZrO<sub>2</sub> exhibits high thermal stability up to 1000°C [17]. CeO<sub>2</sub> is investigated either as a support material or a support promoter as it was found to improve nickel dispersion and oxygen storage capacity [18,19]. Especially CeO<sub>2</sub>-ZrO<sub>2</sub> mixed supports were found to be remarkably active in CO<sub>2</sub> hydrogenation to methane, influencing the surface Ni<sup>2+</sup>/Ni<sup>0</sup> ratio [20]. Mg-Al mixed oxides with mixed periclase-spinel structure have shown high thermal stability. Moreover, the presence of Mg-O groups on the surface provides adequate basic properties. Such catalysts may be obtained through the thermal decomposition of hydrotalcites.

Hydrotalcites are layered hydroxides of bi- and trivalent metal ions with a brucite-like structure where inside the interlayer region anions and water molecules are present. The possibility of introduction of other metallic ions to the brucite-like structure with an atomic radius similar to Mg<sup>2+</sup> and Al<sup>3+</sup>, are beneficial and lead to the formation of complex catalyst. During thermal decomposition, hydrotalcites are decomposed to mixed nano-oxides. In such a way, a strong interaction between the active material and support is obtained, which may result in reduced sintering [21–23].

In CO<sub>2</sub> hydrogenation to methane, several works were already reported either with cobalt as the main active material or as a promoter. Cobalt doping of nickel catalyst was found to improve Ni reducibility resulting in increased activity and selectivity towards methane [24]. Co species allow an increase in hydrogen uptake and Ni-Co synergistic effect was reported for the bimetallic catalyst [25]. Especially at low temperatures, the activity is enhanced. However, this

kind of material was reported to undergo severe sintering [25,26]. On the other hand, Ni-Co materials are resistant to coke formation and stable against metal oxidation [27]. It was also noted, that in comparison to other promoters such as Cu and Fe, Co lowers the activation energy of the reaction due to the reducing nature of cobalt [28]. Several Ni-Co bimetallic systems were already reported as a CO<sub>2</sub> methanation catalysts. Liu et al. tested mesoporous Ni-Co/Al<sub>2</sub>O<sub>3</sub> catalyst, which resulted in high selectivity and stability, especially resistance towards sintering [26]. Similar conclusions were found also by Alrafi et al. for Ni-Co/ $\gamma$ -Al<sub>2</sub>O<sub>3</sub>, which additionally resulted in a satisfactory CO<sub>2</sub> conversion at low temperatures (below 350 °C) [24].

Among the possible solutions, cobalt-promoted hydrotalcites were not extensively studied as a CO<sub>2</sub> methanation catalyst, although they have been examined for application in Fischer-Tropsch synthesis. Co-containing hydrotalcites were successfully tested in reactions such as steam reforming of methane [29,30], ethanol steam reforming [31–33], oxidative ethanol reforming [34], dry reforming of methane [35,36], and other redox processes [37–39]. In bimetallic catalysts, cobalt tends to form an alloy with nickel, which leads to improved electron transfer. It especially enhanced the activity of dehydrogenation [40], which makes it likely to assume that such an effect will be beneficial also for hydrogenation. In reforming reactions, cobalt enhances activity at low temperatures, making it an alternative to noble metals. This effect was assigned to cobalt, which plays the role of an oxidizing agent for the removal of carbon species [41]. This latter reaction is important for preventing catalyst deactivation by coking, together with a high affinity for CO<sub>2</sub> adsorption and strong metal-support interaction [29]. Additionally, hydrotalcite-derived nickel catalysts show satisfactory metal-support interaction, which may prevent cobalt-promoted materials from sintering, which seems to be the biggest obstacle for application of Co as promoter. On the other hand, Ni-Mg-Al hydrotalcites require high temperature of reduction, ca. 900 °C, and possibly introduction of cobalt to the matrix may decrease the reduction conditions, due to the well-known good

reducibility of Co. Moreover, reported in the literature Ni-Co methanation catalysts are supported on alumina – addition of Mg to the matrix should improve surface basicity and convey to better catalytic performance. All the above-mentioned qualities make cobalt-promoted hydrotalcites interesting catalysts for CO<sub>2</sub> hydrogenation to methane.

## 2. Experimental

### 2.1 Catalyst preparation

A series of cobalt-promoted nickel catalysts was prepared via co-precipitation at constant pH (9.5-10) at 65 °C, as proposed by Cavani et al. [23]. The precipitate was aged in the mother solution for 1h, at precipitation temperature, then washed with distilled water, and dried overnight at 80°C in static air. The dried samples were calcined at 500 °C for 5h in static air. The samples contained 15 wt% of nickel in fresh hydrotalcite, and cobalt in amounts of 0, 0.5, 1, 2, and 4 wt%. The amount of nickel and cobalt in calcined samples was calculated based on the assumption that Mg, Al, Ni and Co ions present in the hydrotalcite matrix formed oxides (MgO, Al<sub>2</sub>O<sub>3</sub>, NiO, Co<sub>3</sub>O<sub>4</sub>) during the thermal decomposition [42].

**Table 1.** List of prepared materials and presumed content of active phase in uncalcined (hydrotalcites) and calcined (mixed oxides) samples and content of active phase

Name	Ni/Mg/Al molar ratio	Ni content [wt%]		Co content [wt%]	
		Fresh (calculated)	Calcined (calculated)	Fresh (calculated)	Calcined (calculated)
HTNi15	0.22/0.53/0.25	15.5	20.4	-	-
HTNi15Co0.5	0.22/0.53/0.25	15.5	20.3	0.5	0.7
HTNi15Co1	0.22/0.52/0.25	15.5	20.2	1	1.2
HTNi15Co2	0.22/0.52/0.25	15.4	20.1	2	2.6
HTNi15Co4	0.22/0.50/0.25	15.3	19.7	4	5.1

### 2.2 Physico-chemical characterization

The samples were characterized by XRD, H<sub>2</sub>-TPR, low-temperature N<sub>2</sub> sorption, CO<sub>2</sub>-TPD, XPS, and TEM. X-ray diffraction (XRD) measurements were conducted using a Panalytical Empyrean diffractometer, after each synthesis step (drying, calcination, reduction) and after

catalytic tests. The diffractometer working in Bragg-Brentano  $\theta$ - $\theta$  geometry was equipped with Cu K $\alpha$  ( $\lambda = 1.5406 \text{ \AA}$ ) radiation. The data were collected within a  $2\theta$  range of 3-90 deg. To calculate the Ni crystallite size, the Scherrer equation was utilized, with a correction related to the instrument broadening and shape factor of 0.89 [43]. Low-temperature N<sub>2</sub> sorption measurements were carried out on TriStar 3000 (Micromeritics) to investigate textural properties, such as specific surface area and pore volume. The samples were outgassed for 2 hours at 350 °C beforehand. Temperature programmed reduction (H<sub>2</sub>-TPR) and temperature-programmed desorption (CO<sub>2</sub>-TPD) profiles were obtained using BELCAT-M equipped with a TCD detector. The calcined samples were outgassed for 2 hours at 100 °C before the H<sub>2</sub>-TPR measurement and then reduced at the heating ramp of 10 °C/min, from 100 to 900 °C under a flow of a gas mixture containing 5% H<sub>2</sub> in Ar (50 ml/min). CO<sub>2</sub>-TPD was carried out on the reduced samples, firstly degassed for 2 h at 500 °C and cooled to 80 °C. Secondly, a mixture of 10%CO<sub>2</sub>/He was fed for 1 h to adsorb CO<sub>2</sub> on the sample, and subsequently pure He (50 ml/min) was flowed for 15 minutes to remove weakly adsorbed carbon dioxide. The temperature range of the CO<sub>2</sub>-TPD measurements was from 100 to 800°C with a heating rate of 10 °C/min. The CO<sub>2</sub> uptake was calculated from the number of desorbed volumes of the gas, from the area under the TPD curve. The setup was calibrated prior to the measurement with known amount of CO<sub>2</sub>, to know the precise area of the one pulse, registered with TCD detector.

Transmission electron microscopy (TEM) analyses were carried out with JEM-2010 and JEM-2100Plus (JEOL, Tokyo, Japan) transmission electron microscopes operating at 200 kV for the reduced catalysts. Before measurement, the reduced samples (reduction condition: 900 °C for 1 h in 5 % H<sub>2</sub>/Ar) were dispersed in ethanol before the suspension was added dropwise on a copper grid covered with carbon film. Then the prepared materials were used for the microscopy measurements.

Chemisorption experiments were carried out in a Micromeritics ASAP 2020. 200 mg of a calcined material were loaded into a U-shaped quartz reactor and placed between quartz wool plugs. The catalyst was reduced in situ in pure hydrogen from room temperature to 900 °C at a heating rate of 10 °C/min. After reduction, the sample was treated in helium for 30 min at 900 °C. Thereafter, the material cooled down to 40 °C, and evacuation took place for 30 min. The dispersion (D) of Co and Ni metals was calculated, based on the assumption that two metal sites are covered by one hydrogen molecule. By assuming spherical particles, the particle size ( $d_{Co}$  and  $d_{Ni}$ ) was calculated from D with the following formulas:

$$d_{Co}[\text{nm}] = \frac{96}{D[\%]} \text{ and } d_{Ni}[\text{nm}] = \frac{101}{D[\%]} \quad (1)$$

For a mixture of Ni and Co, the particle size is averaged by:

$$d_{Co-Ni} [\text{nm}] = \frac{96}{D_{Co}} \cdot \frac{Co\%}{100} + \frac{101}{D_{Ni}} \cdot \frac{Ni\%}{100} \quad (2) [44]$$

X-ray photoelectron spectroscopy (XPS) results were obtained with an AXIS Ultra DLD (Kratos Analytical) spectrometer equipped with a magnetic immersion lens and charge neutralization system with a spherical mirror and concentric hemispherical analyzers with monochromated Al anode. All of the recorded data were referenced to the C1s peak at 284.6 eV[45]. Quantitative analysis of the surface composition was determined using the peak areas and the element-specific Scofield factors.

### 2.3 Catalytic tests

The CO<sub>2</sub> hydrogenation to methane was carried out inside a tubular fixed-bed quartz U-type reactor heated by the vertical electric furnace. The temperature was controlled with a K-type thermocouple, placed outside the catalytic bed. The gas composition at the inlet to the reactor was CO<sub>2</sub>/H<sub>2</sub>/Ar = 1.5/6/2.5 with a flow of 100 ml/min (GHSV = 12,000 h<sup>-1</sup>). The products of the reaction (CO<sub>2</sub>, CO, CH<sub>4</sub>, and H<sub>2</sub>) were analyzed with an online micro-chromatograph

(Varian GC4900) equipped with a thermal conductivity detector (TCD). The tests were performed in the temperature range from 250 °C to 450 °C, with the sample kept at steady-state operation for 30 minutes at each temperature. The heating rate between steps was 10°C/min. Prior to the catalytic tests, the materials were reduced for 1h at 900 °C in 5% H<sub>2</sub>/Ar. The stability test was carried out at 300 °C for 5 h, under similar experimental conditions in terms of mixture and GHSV. Equilibrium CO<sub>2</sub> conversion and selectivity to CH<sub>4</sub> were calculated with HSC Chemistry 5.0 software.

CO<sub>2</sub> conversion and CH<sub>4</sub> selectivity were calculated using the equations below:

$$\text{CO}_2 \text{ conversion as } \chi_{\text{CO}_2} (\%) = \frac{F_{\text{CO}_2 \text{inlet}} - F_{\text{CO}_2 \text{outlet}}}{F_{\text{CO}_2 \text{inlet}}} \cdot 100 \quad (3)$$

$$\text{CH}_4 \text{ selectivity as } S_{\text{CH}_4} (\%) = \frac{F_{\text{CH}_4 \text{outlet}}}{F_{\text{CH}_4 \text{outlet}} + F_{\text{COoutlet}}} \cdot 100 \quad (4)$$

Where  $F_{i \text{inlet/outlet}}$  denote the inlet/outlet flow of  $i$  species ( $i = \text{CH}_4, \text{CO}_2, \text{CO}$ ) calculated from the concentration of the gases.

According to M. Boudart, for high conversion, turnover frequency (TOF) should be avoided. Site-time yield (STY), defined as the overall rate of the catalytic reaction within the reactor normalized by the total number of active sites within the reactor [46], was then used and was calculated according to the equation:

$$\text{STY} = \frac{F_{\text{CH}_4}}{m_{\text{cat}}} \left[ \frac{\text{mmol}}{\text{g}\cdot\text{h}} \right] \quad (5)$$

Where  $F_{\text{CH}_4}$  is the flow of methane in the outlet [mmol/h] and  $m_{\text{cat}}$  is a mass of a catalyst [47,48].

The dispersion (D) was also calculated as:

$$D = 6 \frac{\left( \frac{v_m}{a_m} \right)}{d_{va}} \quad (6)$$

Where  $V_m$  is the volume occupied by an atom in bulk metal ( $10.95 \text{ \AA}^3$  for Ni),  $a_m$  is the area occupied by a surface atom ( $6.51 \text{ \AA}^2$  for Ni) and  $d_{va}$  is the mean diameter or metal particle from TEM [49]. To simplify the calculations, the dispersion was defined based on the assumption that we deal with pure Ni particles. This can be explained with the ratio of Ni/Co varying between 5:1 (HTNi15Co4) to 40:1 (HTNi15Co0.5) i.e. Ni atoms are the majority species by far. Such simplification was impossible for  $H_2$ -chemisorption measurement, due to the possible chemical interaction of cobalt with hydrogen.

## Results and discussion

### 2.4 Physico-chemical properties of the hydrotalcite-derived catalysts

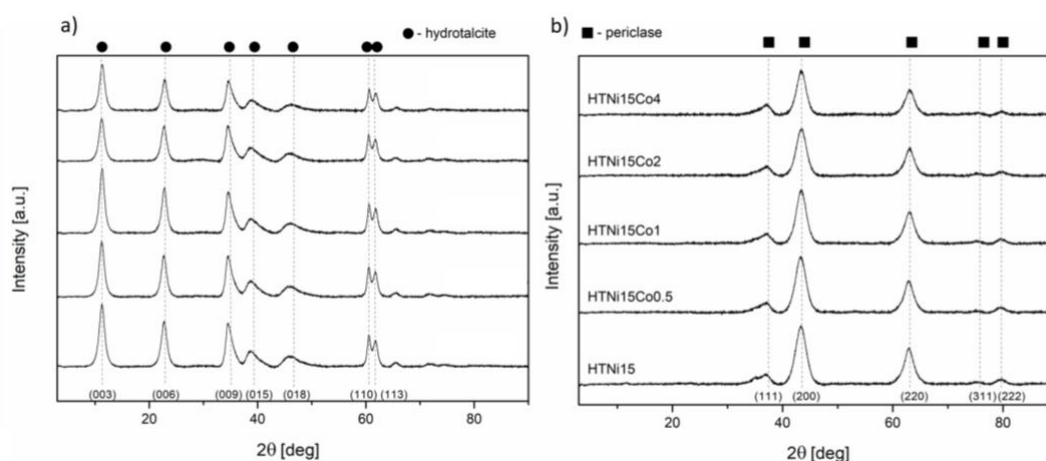
#### 2.4.1. Structural and textural parameters, reducibility, and basic properties of hydrotalcite-derived catalysts

Fig. 1 presents X-ray diffractograms for fresh (1a) and calcined (1b) hydrotalcite-based catalysts. In the Fig. 1a, for a fresh hydrotalcite, a single crystalline phase was detected for all the investigated fresh samples. Detected reflections corresponding to (00*l*) planes at  $2\theta$  of 11.3 deg (003), 22.8 deg (006), and 34.5 deg (009) can be assigned to the multilayered hydrotalcite structure (ICDD 00-022-0700). The lack of secondary phases such as cobalt hydroxide or cobalt oxide may indicate successful incorporation of the promoter to the hydrotalcite structure while the lack of alteration of background signal suggests lack of an amorphous phase, indicating a high level of crystallinity. Hydrotalcite phase-related peaks are broad, suggesting a small size of the crystallites.

The unit cell parameter  $c$  was calculated as proposed by Rives et al. [50], from averaging the position of three reflections corresponding to planes (003), (006), and (009) located at  $2\theta$  range of 10-40 deg as  $c = d_{(003)} + 2d_{(006)} + 3d_{(009)}$ . For all the co-precipitated fresh hydrotalcites, the  $c$  value is in a range of 23.4 to 23.6 Å which confirms a similar extent of electrostatic interaction

inside the investigated structures [34]. Based on the  $c$  parameter, it is possible to define the interlayer anion which for this case is most probably nitrate and/or carbonate with an average distance between the cations of  $3.06\text{\AA}$  for each sample [22].

After calcination at  $500\text{ }^\circ\text{C}$  for 5 h (Fig. 1b), hydrotalcites were decomposed to mixed oxides with periclase-like structure (ICDD 00-045-0946) confirmed with reflections at  $2\theta$  of  $36.9\text{ deg}$  (111),  $42.9\text{ deg}$  (200),  $62.3\text{ deg}$  (220),  $74.7\text{ deg}$  (311) and  $78.6\text{ deg}$  (222). No diffractions lines from additional oxide phases such as nickel or cobalt oxides were detected, which suggests a high degree of phase purity, or their presence in highly dispersed, nano-crystalline form [22,51,52].



**Fig. 1.** XRD diffractograms for (a) dried hydrotalcite-based catalysts; (b) mixed-oxide catalysts after calcination.  $\text{H}_2$ -TPR profiles for calcined hydrotalcites are presented in Fig. 2. All the catalysts show a wide peak in the high-temperature region ( $610\text{--}860\text{ }^\circ\text{C}$ ) assigned to the reduction of nickel species in the periclase-like structure. According to the literature, the observed shift in the peak position was in the direction of lower temperatures with an increase of Co content [26]. The Ni-Co synergistic effect is visible through the improved reducibility of the material [26]. Such a trend is observed also for the as-prepared materials, excluding sample HTNi15Co1, for which the center of the peak is at a temperature  $10\text{ }^\circ\text{C}$  higher than for the unpromoted material. This indicates strong Ni-O interactions inside the matrix [27] or can be related to the residual

hydrotalcite phase detected only in this sample [53]. For the cobalt-promoted material, small peaks at low temperatures were registered. They are probably originating from the reduction of small amounts of  $\text{Co}_3\text{O}_4$ , reducible at temperatures 270-400°C [54,55]. The peaks at 290-310°C may be assigned to weakly bonded and well-dispersed cobalt (III) oxide while those in the range 370-410°C originate from the reduction of  $\text{Co}^{3+}$  ions dissolved in Mg-Al oxide matrix, reduced to  $\text{Co}^{2+}$  [30,56]. The remaining cobalt is probably reduced with nickel above 600°C [57,58].

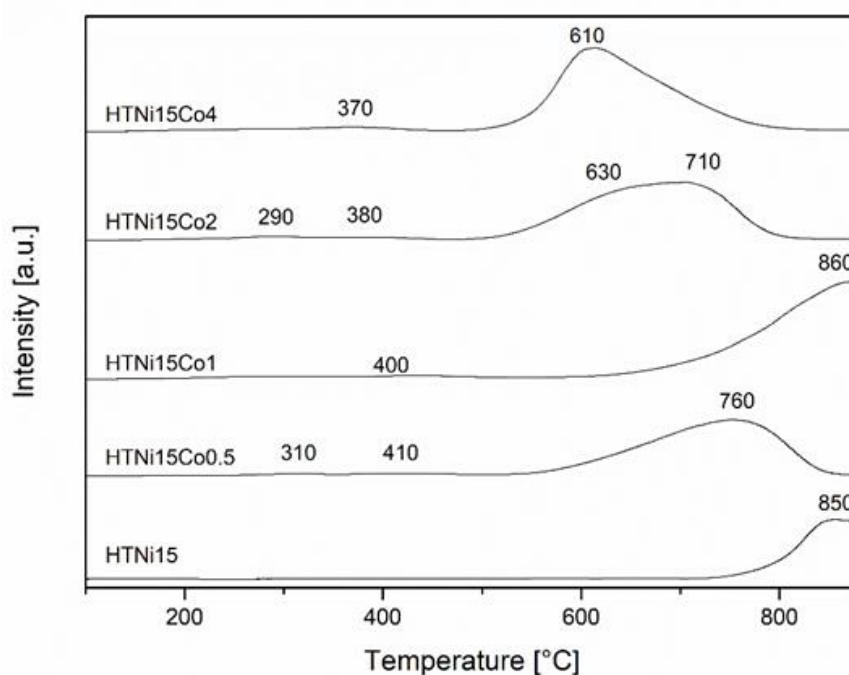


**Fig. 2.** H<sub>2</sub>-TPR profile for calcinated hydrotalcites based catalysts

Low-temperature  $\text{N}_2$  sorption was carried out to investigate the textural properties of the examined materials. The isotherms are reported in Fig. S1. All the hydrotalcite-derived catalysts have the shape of the isotherm typical for this kind of mesoporous materials, classified as type IV according to IUPAC [59]. All the promoted materials can be characterized with H1 subtype of isotherm, which suggests cylindrical and well-defined pores. Textural properties are presented in Table 2. Specific surface area  $S_{\text{BET}}$  for the examined samples is ca. 190-220  $\text{m}^2/\text{g}$  for promoted materials and ca. 250  $\text{m}^2/\text{g}$  for the unpromoted. Additionally, shape of the hysteresis loop for the HTNi15 samples is slightly different, than for the promoted materials –

it suggests change of the shape of pores in the direction of more regular and cylindrical, with the addition of cobalt. With the presence of cobalt, a decrease in specific surface area is visible, although smaller than the experimental error for low-temperature N<sub>2</sub> sorption. A change in the porous properties of the hydrotalcite-derived materials is also observed with the increase of cobalt promotion. For all the samples, total pore volume is practically dominated by mesopores, as confirmed by the type IV isotherm. A total pore volume of 0.65 cm<sup>3</sup>/g was found for the HTNi15 sample, decreasing to 0.35 cm<sup>3</sup>/g for HTNi15Co4. For the samples the mean pore diameter was decreasing with the increase of cobalt promotion, with small abbreviation for HTNi15Co2 sample, where mean pore diameter was larger than for neighboring samples. Such trend may be assigned to the blockage of mesopores. In general, with increasing cobalt content, a trend indicating decrease of porosity is visible. This effect has often been observed in the literature for transition metal-promoted Ni/Mg/Al hydrotalcites, in which the promoter was blocking the pores [60,61].

**Table 2.** Specific surface area and porous properties of the calcined catalysts

Sample	S <sub>BET</sub> [m <sup>2</sup> /g]	Total pore volume [cm <sup>3</sup> /g]	d <sub>p</sub> [nm]	V <sub>mesopores</sub> [cm <sup>3</sup> /g]
HTNi15	256	0.65	14	0.62
HTNi15Co0.5	215	0.49	13	0.47
HTNi15Co1	213	0.50	10	0.49
HTNi15Co2	194	0.35	11	0.33
HTNi15Co4	212	0.35	9	0.33

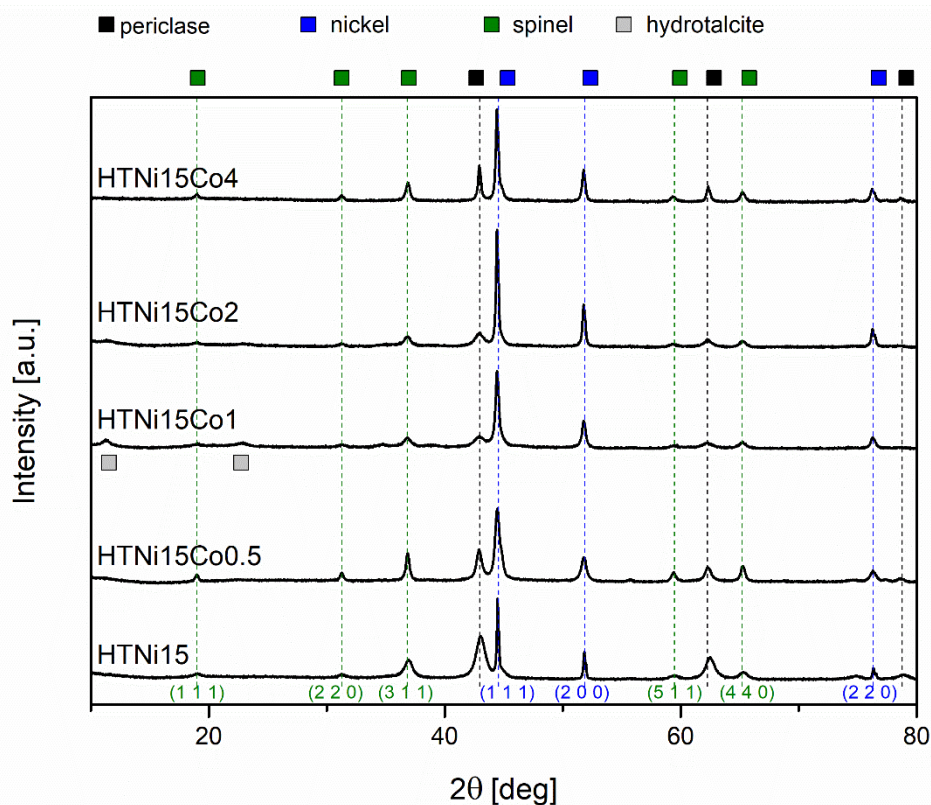


**Fig. 3.** X-ray diffractograms for the reduced hydrotalcite-derived catalysts

X-ray diffractograms for the reduced hydrotalcite-derived materials are presented in Fig. 3. Three crystalline phases are distinguished, which are periclase (ICDD 00-045-0946) already discussed in Fig. 1, spinel (ICDD 01-070-5187), and metallic nickel (ICDD 03-065-0380). The nickel phase originates from the reduction of nickel species present in the periclase-like structure and was confirmed with three sharp reflections at  $2\theta$  of 44.3 (111), 51.7 (200), 76.1 (220), typical for a metallic nickel. Spinel is usually formed at high temperatures (above 700°C), so most probably this phase was formed from periclase-like oxide during the reduction step at 900°C. Most probably the obtained spinel oxide is  $\text{MgAl}_2\text{O}_4$ , as confirmed by the reflections at  $2\theta$  of 19.0 deg (111), 31.3 deg (220), 36.8 deg (311), 44.8 deg (400), 59.3 deg (511), and 65.2 deg (440). The spinel formation is not always registered during the reduction of hydrotalcites at 900°C, also catalysts with only periclase oxide structure have been reported [22].

Fig. S2 illustrates CO<sub>2</sub>-TPD profiles for the reduced hydrotalcite-derived materials. The profiles were deconvoluted into three Gaussian curves with centers of the desorption peaks in the range 120-150°C for weak basic sites, 185-235°C for medium-strength basic sites, and 285-345°C for strong basic sites [62]. In the unpromoted HTNi15 samples, the fraction of each type of basic sites is similar. The low-loading promotion with cobalt (0.5-2 wt%) leads to a significant increase in the number of medium-strength and strong basic sites. The HTNi15Co4 sample with the highest content of cobalt resulted in a lower number of sites than in the unpromoted catalyst, but with a uniform share of the strength of sites. Additionally, after the incorporation of cobalt, a shift in desorption temperature in each range is also observed (cp. CO<sub>2</sub>-TPD profiles, Fig. S3). The desorption temperature for weak, medium-strength and strong basic sites decreased respectively by ca. 20, 30, and 50 °C for the HTNi15Co0.5 catalyst, in comparison to HTNi15. With the increase in the amount of cobalt promotion, the temperature of the desorption peak center increases, suggesting a strengthened interaction between CO<sub>2</sub> and the site. The 3d orbitals of both metallic nickel and cobalt are not fully occupied with electrons, which may promote activation of CO<sub>2</sub> to form CO<sub>2</sub><sup>-</sup>. As a result, Ni and Co form a Lewis basic complex with the hydroxyl surface group. Such interaction with CO<sub>2</sub> shifts the desorption temperature to a higher range [54].

**Table 3.** The distribution of basic centers (from CO<sub>2</sub>-TPD) of the reduced catalysts

	<b>Weak</b> [μmol/g]	<b>Medium</b> [μmol/g]	<b>Strong</b> [μmol/g]	<b>Total</b> [μmol/g]	<b>Weak</b> [%]	<b>Medium</b> [%]	<b>Strong</b> [%]
<b>HTNi15</b>	23	25	25	74	31	35	34
<b>HTNi15Co0.5</b>	10	78	82	170	6	46	48
<b>HTNi15Co1</b>	18	66	94	178	10	37	53
<b>HTNi15Co2</b>	10	54	51	116	9	47	44
<b>HTNi15Co4</b>	16	35	44	95	17	37	47

It was already reported that basicity can be linked with the catalytic performance for CO<sub>2</sub> methanation. Especially medium-strength basic sites were related to improved CO<sub>2</sub> conversion

[22]. In the case of nickel catalyst, the number of these sites can be increased by increasing the nickel content or by addition of the optimal amount of a structural promoter such as copper, iron, lanthanum, vanadium, etc. [8,53,60,63].

### **2.4.3. Transition Electron Microscopy and Surface analyses of Co-Ni hydrotalcite-derived catalysts**

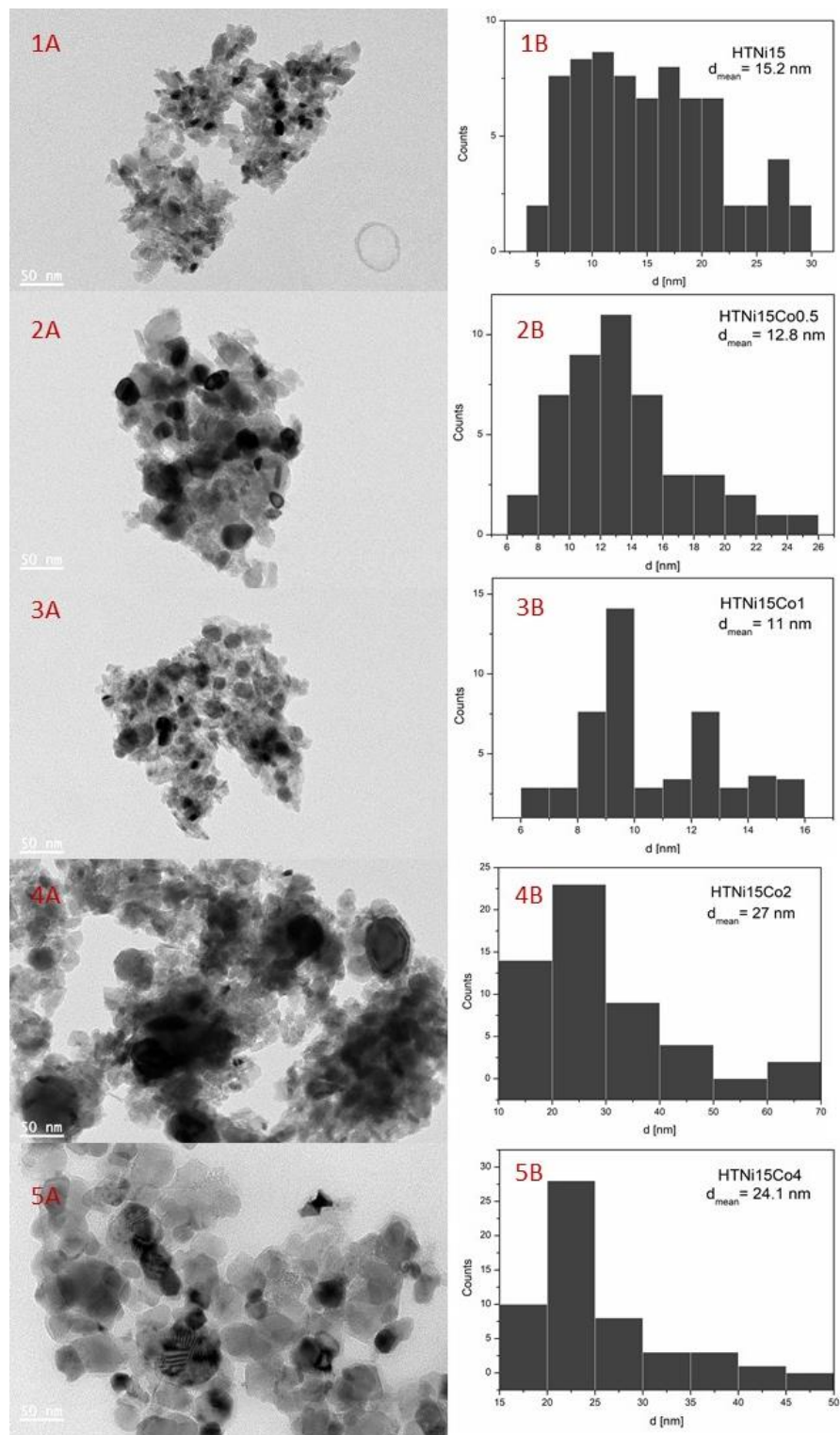


**Fig. 4.** 1-5(a) - Transmission Electron Microscopy (TEM) images of reduced hydrotalcite-derived catalysts; 1-5(b) – histograms with particle size distribution for the studied materials.

TEM measurements were carried out to determine the nickel particle size in the studied catalysts. From Fig. 4, one can see that the most uniform distribution of nickel particles was obtained for the HTNi15Co1 sample. In this catalyst, small nickel particles with a relatively

narrow size distribution are identified. With the increase in cobalt content, the nickel particle size is significantly increasing. The Ni particle size distribution for the samples such as HTNi15Co2 and HTNi15Co4 is quite wide, including particles with sizes of ca. 10-15 nm and 60-70 nm with dominating crystallites of ca. 20-30 nm. The presence of 2-3 times larger particles is in general not beneficial. It is well known that large Ni particles are prone to coking, and result in less availability of active sites. HTNi15Co0.5 catalyst shows small nickel particles on the surface, but some bigger particles are also present. The average diameter of nickel particles for this sample is ca. 12.8 nm. The unpromoted catalyst (HTNi15) is characterized by a uniform distribution of nickel particles, with an average diameter of ca. 15 nm. For the majority of samples, the obtained TEM average particle diameter values are close to those calculated from Scherrer's equation, based on XRD (Table 9).

XPS was performed to analyze the oxidation state of nickel and cobalt in the reduced hydrotalcite-derived materials. Fig. 5(a) presents fragments of the spectra corresponding to the binding energy of nickel.

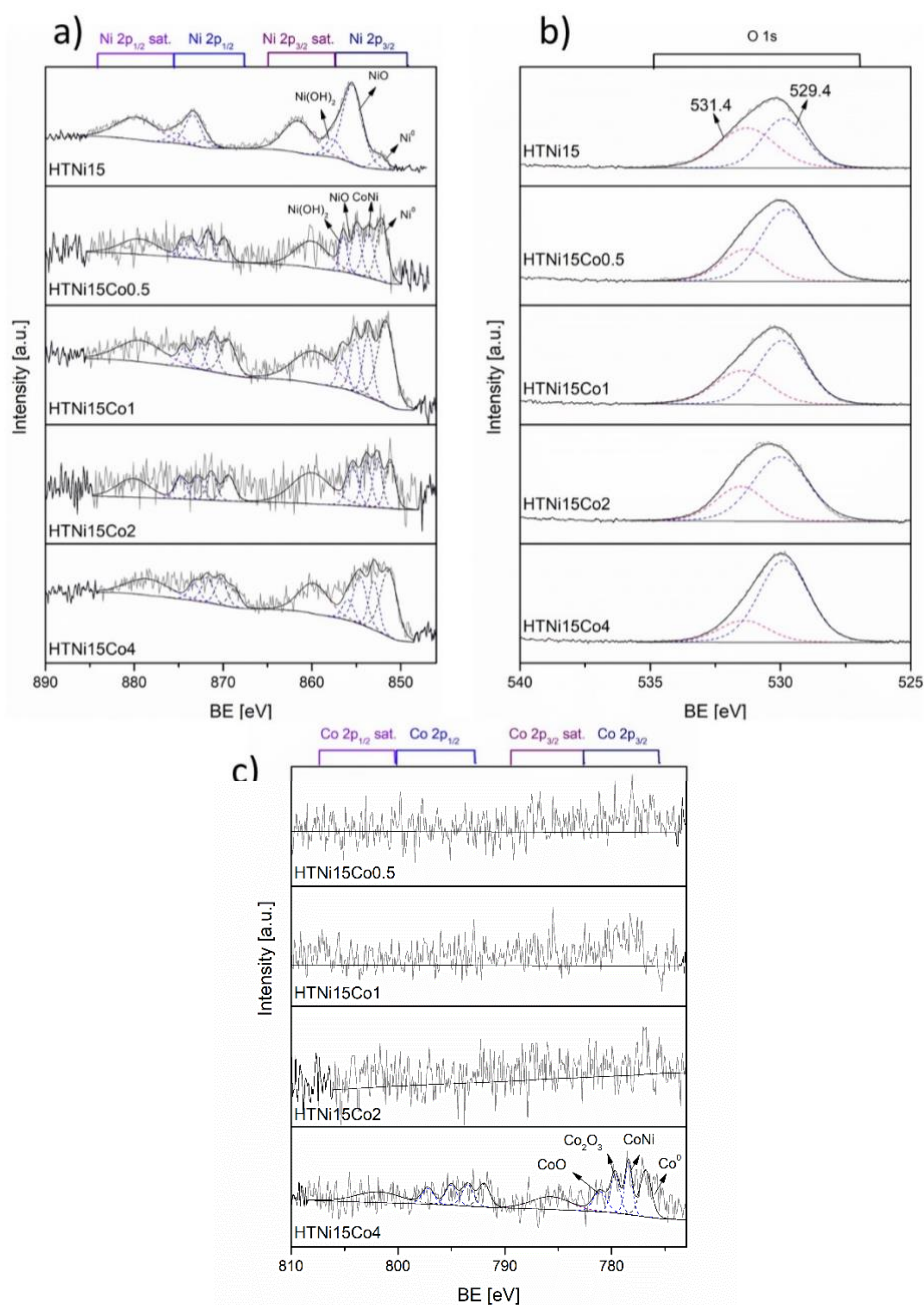


**Fig. 5.** XPS spectra for hydrotalcite-derived catalysts (a) regions of Ni 2p, (b) regions of Co 2p, (c) regions of O 1s

After deconvolution of the Ni 2p<sub>3/2</sub> peak (Fig. 5(a)) for the HTNi15 sample, it may be assumed that the Ni 2p<sub>3/2</sub> peak is composed mostly of energies resulting from Ni<sup>0</sup> (peak at ca. 852.3 eV [64]), Al<sub>2</sub>NiO<sub>4</sub> at 857.0 eV [65], and NiO at 855.4 eV [66]. The main peak assigned to Ni 2p<sub>3/2</sub> is located at 855.5 eV for the HTNi15 sample and shifts to lower energies with the increase of cobalt content, up to 854.2 for HTNi15Co4. This may indicate electron transfer from Ni species resulting in higher electron density, related to the formation of a CoNi solid solution [26]. The

appropriate satellite peaks are located at ca. 5.5 eV above the main peak [66]. For the cobalt promoted samples, it was possible to distinguish the fourth peak at 852.9-853.1 eV. In all the Co-containing samples, the peak area corresponding to NiO is ca. 18-25% of the area of the whole peak, while it reaches ca. 78% for the unpromoted. The surface content of the Ni(OH)<sub>2</sub> phase is present in ca. 10-20% in each sample. It was probably formed in parallel to NiO, from contact with air during transportation of the reduced sample before the actual measurement [67]. The metallic Ni<sup>0</sup> species are present in ca. 38-50% in the Co-promoted catalyst. The highest amount of ca. 49% was observed in HTNi15Co1. The catalyst with the smallest contribution from metallic nickel detected on the surface was HTNi15, containing only 8% of Ni. For the samples with the addition of cobalt, the peak with binding energy higher than that of Ni<sup>0</sup> can most likely be assigned to the Ni-Co solid solution of those two elements [68]. The content in the materials is similar, ca. 20%. The above results suggest that nickel is present mainly in reduced, metallic form or together with cobalt in the solid solution.

Figure 5(c) presents the cobalt 2p region. For all the samples except HTNi15Co4, due to the low presence of cobalt, it was impossible to deconvolute representative peaks. However, for higher cobalt loadings the main Co 2p<sub>3/2</sub> peak was located at ca. 780 eV with a corresponding satellite located 6.0 eV above the main peak [69]. The Co 2p<sub>1/2</sub> peak had a maximum at ca. 796 eV with a satellite at 802 eV. Moreover, more particularly on HTNi15Co4, four oxidation states were distinguished from the Co 2p<sub>3/2</sub> peak, as assigned to Co<sub>2</sub>O<sub>3</sub> at ca. 780 eV, CoO at ca. 781.2 eV, Co<sup>0</sup> at ca. 777.3 eV, and Co-Ni at ca. 778.4 eV [28,68–70]. For the peak assigned to metallic cobalt, we can assume that a shift in the direction of higher energies was detected - from 778.0 eV in HTNi15Co0.5 to 778.5 eV at HTNi15Co4, which suggests the formation of the solid solution between nickel and cobalt. This is especially visible for the sample with the highest concentration of Co [25]. The peak assigned to Co<sub>2</sub>O<sub>3</sub> contributes to ca. 18-25% of the cobalt phase in the deconvoluted Co 2p<sub>3/2</sub> peak. Probably this oxide was partially formed from contact

with air during transportation.  $\text{Co}^{2+}$  cobalt originating from  $\text{CoO}$  was likewise partially formed before the XPS measurement.

Furthermore, the peak related to O 1s is for all samples located at ca. 530.4 eV (Fig. 5(b)). The peak can be deconvoluted into two Gaussian curves, one with the maximum at 529.4 eV corresponding mostly to the NiO phase [71] and to the cobalt oxides which give a peak at similar binding energy [72]. The second peak at 531.4 eV was assigned most probably to -O-H groups present in the material as  $\text{Ni}(\text{OH})_2$ , formed during contact of the sample with atmospheric air [73].

The relative area of  $2p_{3/2}$  peaks of nickel is presented in Table 4. As mentioned before, the samples were partially oxidized during contact with air. The highest amount of nickel oxide phase was detected in the unpromoted catalyst. Based on the results reported in Table 4, it may be deduced that the presence of cobalt influences the nickel oxidation state – the majority of nickel is present in the reduced form which can be assigned to the improved reducibility ensured by cobalt addition.

**Table 4.** The relative area of Ni  $2p_{3/2}$  peaks for hydrotalcite-derived samples based on XPS measurement

	<b>HTNi15</b>	<b>HTNiCo0.5</b>	<b>HTNiCo1</b>	<b>HTNiCo2</b>	<b>HTNiCo4</b>
<b>Ni<sup>0</sup></b>	8	38	49	39	45
<b>Ni-Co</b>	-	21	21	19	20
<b>NiO</b>	78	25	19	21	25
<b>Ni(OH)<sub>2</sub></b>	14	16	11	21	10

## **2.5 CO<sub>2</sub> catalytic methanation and structure-activity analysis**

### **2.5.1. On the effect of the temperature**

Results of the catalytic tests towards the methanation reaction are presented in Fig. 6. Due to the construction of the experimental setup, the expected temperature of the catalytic bed deviates from the actual temperature measured with the thermocouple in the high-temperature range of the measurements (400-450°C). The presented results are in agreement with the

temperature measured at 1 mm of the catalytic bed. CO<sub>2</sub> conversions (Fig. 6(a)) obtained for all the Co-promoted hydrotalcite-derived catalysts are higher in the entire temperature range than the conversion levels obtained for the unpromoted HTNi15 sample. At 250°C none of the catalysts are exceeding 25% of CO<sub>2</sub> conversion. An increase in temperature to 300°C resulted in a significant leap in the activity for samples with 0.5, 1, and 2 wt% of Co. The best catalytic performance was obtained for the HTNi15Co1 catalyst, which shows conversions close to the thermodynamic equilibrium at 350°C and above. HTNi15Co0.5 and HTNi15Co2 show similar activity throughout the temperature range, almost reaching the thermodynamical equilibrium at 400°C. In comparison to the best sample, the catalysts promoted with 0.5 and 2wt% of cobalt showed only a few percent lower conversions. Among the Co-containing materials, the worst performance was registered for HTNi15Co4, which did not reach CO<sub>2</sub> conversion close to equilibrium in the entire temperature range. Values of CO<sub>2</sub> conversion and CH<sub>4</sub> selectivity are compared in the Table 5.

The selectivity towards CH<sub>4</sub> formation, presented in Fig. 6(b), confirms the good performance of cobalt as a promoter for CO<sub>2</sub> methanation. Thus, at 250°C, HTNi15Co0.5, HTNi15Co2, HTNi15Co4 showed the formation of carbon monoxide (23-50%), whereas both HTNi15 and HTNi15Co1 gave high selectivity to methane (92-96%). At temperatures higher than 300°C, all the catalysts were selective for methane, with a CH<sub>4</sub> selectivity not falling under 94%, and reaching ca. 97-99% for all the Co-containing materials.

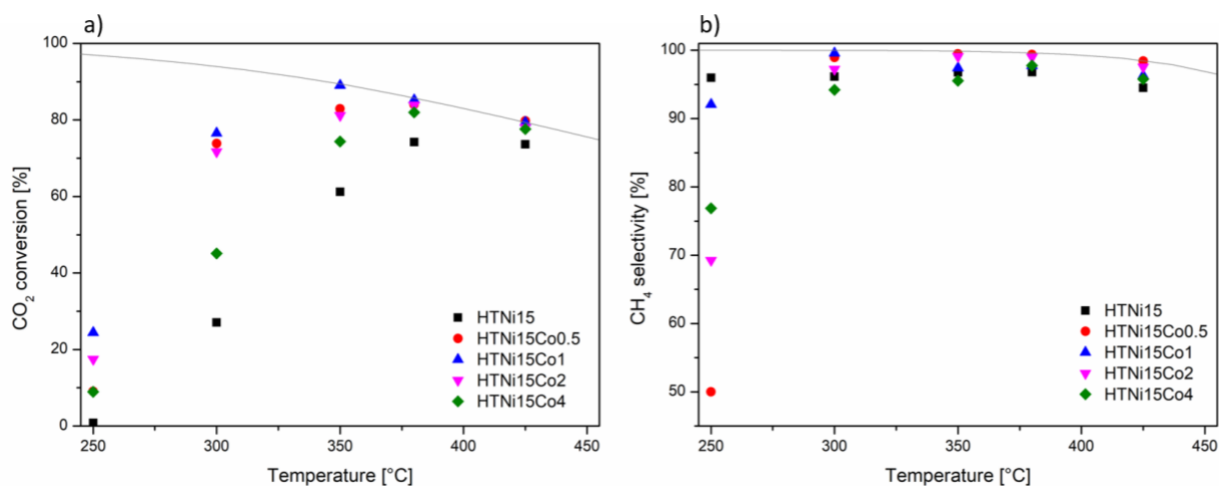


**Fig. 6.** (a) CO<sub>2</sub> conversion as a function of temperature; (b) CH<sub>4</sub> selectivity as a function of temperature for hydrotalcite-derived catalysts

**Table 5.** CO<sub>2</sub> conversion and CH<sub>4</sub> selectivity registered for hydrotalcite-derived catalysts

Temperature [°C]	CO <sub>2</sub> conversion [%]					CH <sub>4</sub> Selectivity [%]				
	HTNi15	HTNi15Co0.5	HTNi15Co1	HTNi15Co2	HTNi15Co4	HTNi15	HTNi15Co0.5	HTNi15Co1	HTNi15Co2	HTNi15Co4
250	1	9	24	17	9	96	50	92	69	77
300	27	74	77	72	45	96	99	99	97	94
350	61	83	89	81	74	97	99	97	99	95
385	74	84	85	84	82	97	99	98	99	98
430	74	80	79	78	77	94	98	96	97	96

### 2.5.2. On the effect of time on stream

A stability test of 5 hours was carried out at 300 °C for all the examined catalysts (Fig. 7(a)). Moreover, for the promoted catalyst showing the best activity, a 24h stability test was also performed at the same temperature. It is worth noting that the cobalt-containing samples remained stable during TOS. HTNi15Co1 did not lose activity during 24 hours on stream while CO<sub>2</sub> conversion decreased by 1-1.5 % for unpromoted HTNi15 (Fig. 7(b)). The cobalt-promoted catalyst was already reported as the most stable, in comparison to Fe and Cu for NiO-MgO systems [28].

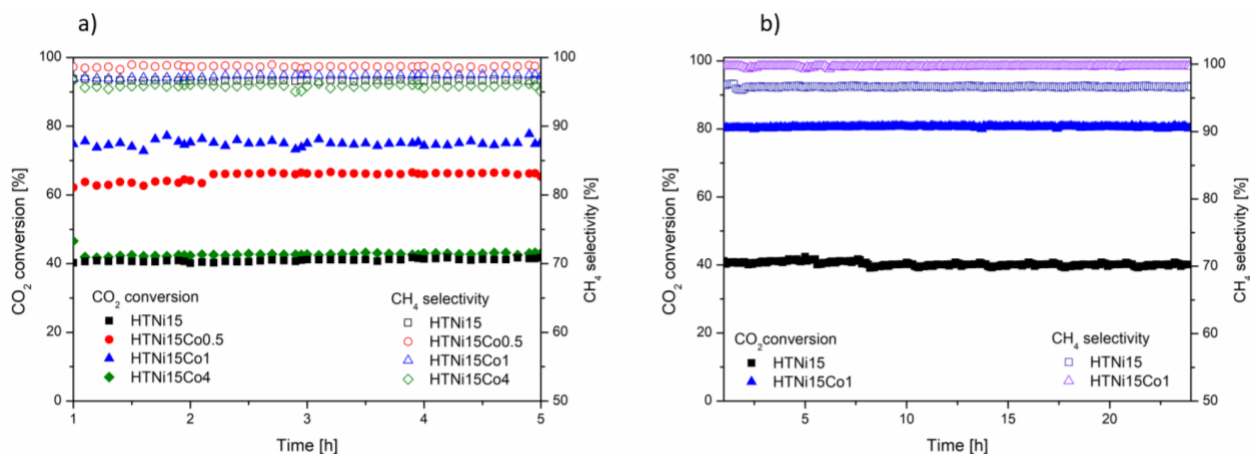


**Fig. 7.** (a) CO<sub>2</sub> conversion and CH<sub>4</sub> selectivity at 300°C during 5h stability test; (b) CO<sub>2</sub> conversion and CH<sub>4</sub> selectivity at 300°C during 24h stability test for the hydrotalcite-derived samples

Ni<sup>0</sup> particle size on reduced samples was determined using Scherrer's equation based on XRD measurement (medium value of crystallite size for all the significant nickel reflections at 44.44, 51.78, and 76.27 deg.), H<sub>2</sub>-chemisorption, and TEM. Ni<sup>0</sup> Values are compared in Table 6. The general tendency is similar for all studied samples. The smallest particles (11-13 nm) were detected for low loading cobalt catalysts, such as HTNi15Co0.5 and HTi15Co1. The largest (24-27 nm) nickel crystallites were found in samples with higher cobalt content: HTNi15Co2 and HTNi15Co4. An intermediate size (15 nm) was found in the unpromoted material. These results confirmed that the promotion of Ni catalyst by Co led to the formation of large Ni particles as already discussed [25,26]. Furthermore, for HTNi15Co1 and HTNi15Co2, the crystallite sizes obtained via chemisorption and XRD vary significantly. Although for the latter catalyst, the XRD result is confirmed by TEM. In this sample, the distribution of particle size was very wide and both nanometric crystallites and larger agglomerates were present on the surface. Considering the results, the most reliable is the particle size result obtained via TEM. Nickel crystallite size calculated from XRD is an average value, dependent additionally on the experimental set-up: calibration, chosen shape factor, limitations in detection of the crystallites below 4 nm, etc.

The nickel dispersion for the investigated catalysts is listed in Table 6. The dispersion values obtained with H<sub>2</sub>-chemisorption and TEM are having a similar sequence, but due to uncertainties, the values are slightly different since hydrogen spillover on the support may occur during H<sub>2</sub> chemisorption [74]. Likewise, H<sub>2</sub>-chemisorption measurements were performed in the atmosphere of pure hydrogen, while samples were normally reduced at the mixture of 5% H<sub>2</sub>/Ar, which may explain the observed differences. On the other hand, with H<sub>2</sub>-chemisorption it is not possible to detect buried particles, which can be achieved with TEM [75]. Additionally, choosing optimal temperature conditions for H<sub>2</sub>-chemisorption measurement on bimetallic Ni-Co catalyst is difficult. Near zero activation energy of hydrogen adsorption at 300 K for nickel, and a kinetic barrier at low temperature for cobalt (for which recommended measurement temperature is 400 K) may affect the adsorption of a well-established monolayer. However, it was already reported that with an increase of the amount of cobalt promoter in nickel catalyst, the dispersion value obtained via H<sub>2</sub>-chemisorption is decreasing [44,76]. Results obtained with H<sub>2</sub> chemisorption are however in agreement with the sequence for catalytic activity – HTNi15Co1 (11.8%) > HTNi15Co0.5 (10.5%) > HTNi15Co2 (5.5%) > HTNi15Co4 (4.7%) > HTNi15 (3.2%). This may be assigned to overall hydrogen uptake on the surface of the catalyst, rather than particle size itself. In comparison, the highest dispersion according to crystallite size based on TEM images was obtained on the most active sample HTNi15Co1 (8.6%). Slightly lower dispersion of 7.9% was found in the second-best material HTNi15Co0.5. The unpromoted catalyst resulted in a dispersion of 6.7%, which is higher than the dispersion for HTNi15Co4 (4.2%). Site time yield (STY) values calculated for reaction at 300 °C are reported in Table 6. STY was defined as the number of molecules of a specified product obtained per mass of catalyst and per unit time [77]. STY values seem more valid for this kind of study, when CO<sub>2</sub> is formed in several reactions, not allowing for a precise definition of TOF. Catalysts with Co content 0.5-1 wt% resulted in STY values higher than for

other materials, of  $76.63 \text{ mmol}\cdot\text{g}^{-1}\cdot\text{h}^{-1}$  for HTNi15Co0.5 and  $49.64 \text{ mmol}\cdot\text{g}^{-1}\cdot\text{h}^{-1}$  for HTNi15Co1. According to this result, the highest yield of methane formation was obtained for a sample with 0.5 wt% of cobalt, due to the lowest density of this catalyst. The remaining samples HTNi15, HTNi15Co2, and HTNi15Co4 resulted in similar STY values of 27.28, 25.59, and  $24.39 \text{ mmol}\cdot\text{g}^{-1}\cdot\text{h}^{-1}$  subsequently.

**Table 6.** The particle size of  $\text{Ni}^\circ$  of reduced catalysts calculated from XRD, TEM,  $\text{H}_2$ -chemisorption; dispersion calculated from TEM and  $\text{H}_2$ -chemisorption measurements; Site Time Yields calculated at  $300^\circ\text{C}$

	HTNi15	HTNi15Co0.5	HTNi15Co1	HTNi15Co2	HTNi15Co4
<b>Ni<sup>°</sup> particle size (XRD) (nm)</b>	15	12	16	27	21
<b>Ni<sup>°</sup> particle size (TEM) (nm)</b>	15	13	11	27	24
<b>Ni<sup>°</sup> particle size (H<sub>2</sub>-Chemisorption) (nm)</b>	17	10	9	18	22
<b>Dispersion calculated from H<sub>2</sub>-chemisorption (%)</b>	3.2	10.5	11.8	5.5	4.7
<b>Dispersion calculated from TEM (%)</b>	6.7	7.9	8.6	3.7	4.2
<b>STY [<math>\text{mmol}\cdot\text{g}^{-1}\cdot\text{h}^{-1}</math>] Calculated from TEM</b>	27.28	76.63	49.63	25.59	24.39

In comparison to other promoters used with Ni-hydroxalcalite-derived catalysts (Table 7) cobalt is one of the most promising promoters. As reported in Table 7, at similar conditions at  $300^\circ\text{C}$ , the promotion with 1 wt.% of cobalt is comparable to 2 wt% of vanadium and 1.5 wt% of iron.  $\text{CO}_2$  conversion reached ca. 75-79% with close to equilibrium selectivity to methane for all presented catalysts. Cobalt may be an interesting alternative for the iron-doped hydroxalcalites. Iron promotion provides better dispersion of nickel, but cobalt-promotion results in higher basicity and improved reducibility. It should be mentioned, however, that lanthanum and yttrium showed better activity than the Co-promoted hydroxalcalite-based catalysts studied in this work. Thus,  $\text{CO}_2$  conversion of 80% and 88% were obtained for 0.4 wt% of La and 0.4% of Y

in a 20 wt% Ni catalyst with selectivity to CH<sub>4</sub> close to 100%. However, the effect of these promoters on hydrotalcite-based catalysts was not tested for 24h runs. Furthermore, copper addition is not as effective in CO<sub>2</sub> methanation as other promoters, and similarly as vanadium, in increased concentrations promotes the reverse water-gas shift reaction (RWGS) [53].

**Table 7.** Comparison with other hydrotalcite-derived catalysts for CO<sub>2</sub> methanation with nickel content ca. 20 wt%

No.	Ni content [wt%]	Promoter	CO <sub>2</sub> conversion [%]	CH <sub>4</sub> Selectivity [%]	Conditions	Reference
1	21	La 0.4%	80	99	t=300°C GHSV= 12 000 h <sup>-1</sup> H <sub>2</sub> /CO <sub>2</sub> =4	[8]
2	15	V 2%	75	99	t=300°C GHSV= 12 000 h <sup>-1</sup> H <sub>2</sub> /CO <sub>2</sub> =4	[53]
3	20	Cu 1%	61	98	t=300°C GHSV= 12 000 h <sup>-1</sup> H <sub>2</sub> /CO <sub>2</sub> =4	[63]
4	20	Fe 1.5%	79	99	t=300°C GHSV= 12 000 h <sup>-1</sup> H <sub>2</sub> /CO <sub>2</sub> =4	[60]
5	n.m.	Ru 0.5%	86	99	t=350°C GHSV= 24 000 h <sup>-1</sup> H <sub>2</sub> /CO <sub>2</sub> =4	[78]
6	16-20	Y 0.4%	88	98	t=300°C GHSV= 12 000 h <sup>-1</sup> H <sub>2</sub> /CO <sub>2</sub> =4	[79]
7	20	Co 1%	77	99	t=300°C GHSV= 12 000 h <sup>-1</sup> H <sub>2</sub> /CO <sub>2</sub> =4	This work

\*n.m. – not mentioned

### 2.5.3 Structure-reactivity analysis of Co-promoted hydrotalcite-derived Ni catalysts

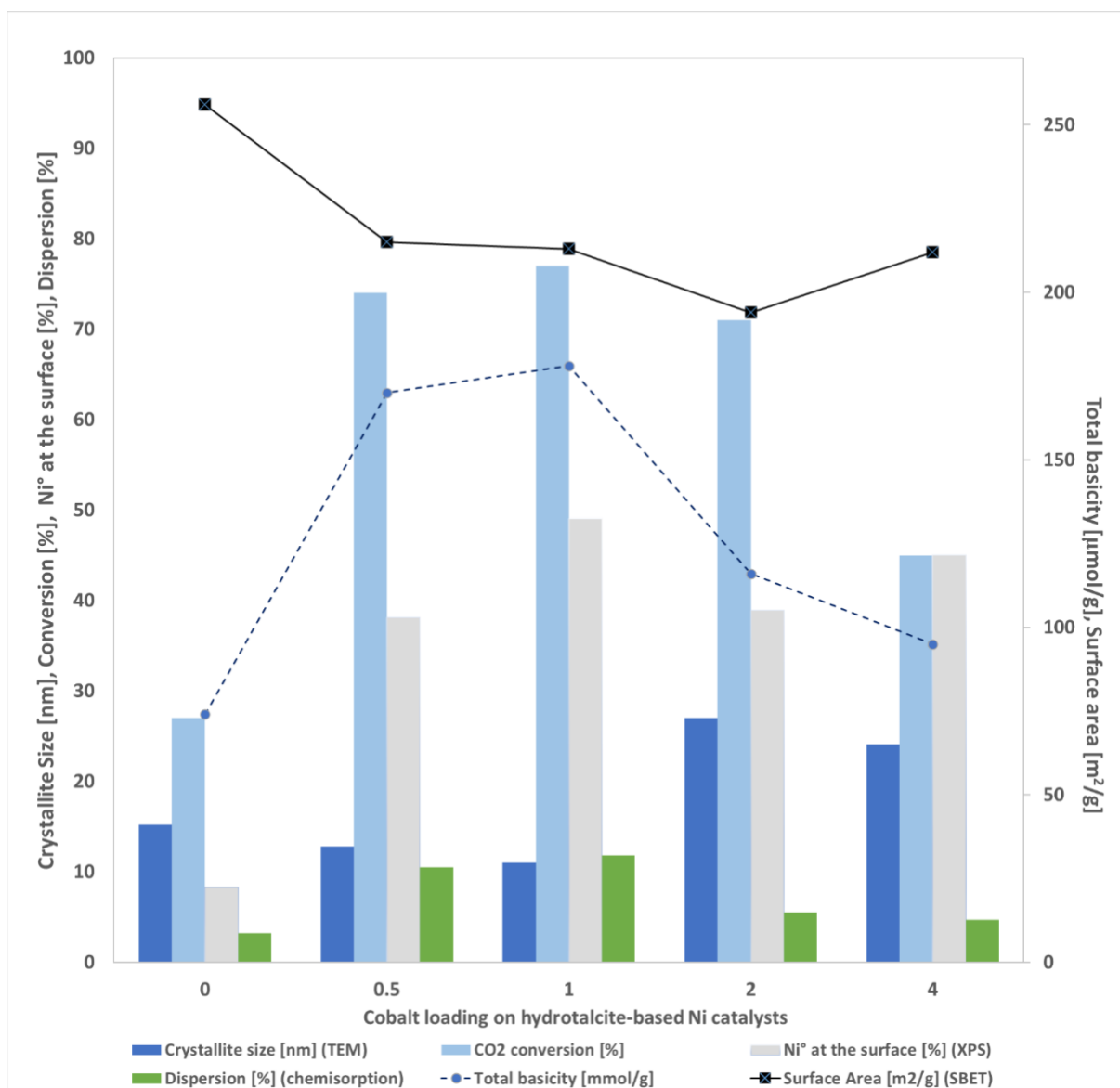


**Fig. 8.** Correlation between particle size from TEM [nm], CO<sub>2</sub> conversion at 300°C, a fraction of Ni<sup>0</sup> at the surface [%], dispersion from H<sub>2</sub> chemisorption [%], total basicity [μmol/g], and specific surface area [m<sup>2</sup>/g] for the hydrotalcite-derived catalysts

From Fig. 8, one can see a direct correlation between catalytic activity and the number of basic sites on the surface. The most active was the sample with the highest total number of basic sites and the highest number of strong basic sites. In the case of the total number of sites, the order of the samples with the highest to the lowest number is the same as the order for samples at 300°C from the most active to the least active, which is HTNi15Co1 > HTNi15Co0.5 > HTNi15Co2 > HTNi15Co4 > HTNi15. Since the fraction of weak basic sites in the promoted samples was negligible in comparison to medium-strength and strong, it is possible to conclude that the content of the latter is most influential for the catalytic activity. The presence of cobalt

increased the strength of the basic sites on the surface which was beneficial for the catalytic performance in this case.

The most active catalysts – HTNi15Co0.5 and HTNi15Co1 were also those which present the smallest size of nickel crystallites. Although in the case of other catalysts – HTNi15Co2 and HTNi15Co4, the correlation between nickel particle size and catalytic activity is not so evident. A direct correlation is visible between catalytic activity and dispersion calculated from H<sub>2</sub> chemisorption measurements, which is related rather to the hydrogen uptake on the catalyst, than to the actual particle size obtained with this method.

The specific surface area decreases with the increase of cobalt content. There is a certain tendency that the catalysts with higher surface area and lower amounts of cobalt were found to be more active. The best catalytic performance was also observed for materials with the better reducibility of nickel at the surface, as confirmed by XPS. Thus, for HTNi15Co1 which was also the most active, the Ni<sup>0</sup> amount at the surface was 49%. Furthermore, the ranking of Ni<sup>0</sup> at the surface was as follows: HTNi15Co0.5 (38% Ni<sup>0</sup>), HTNi15Co2 (39% Ni<sup>0</sup>), HTNi15 (8% Ni<sup>0</sup>), which is in line with the catalytic activity (Fig. 8).

The beneficial influence on the catalytic performance of the Ni-Co solid solution formation in the bimetallic catalyst has been widely reported in the literature [26]. However, our data do not clearly confirm such correlation. According to the XPS results, for the higher loading in Co, the presence of a Ni-Co phase was identified. Considering the cobalt loading on the catalysts, it is hard to speculate on the role of cobalt species, since it is well known that Ni<sup>0</sup> are the active sites for the methanation reaction. However, from CO<sub>2</sub>-TPD, low-temperature N<sub>2</sub> sorption, and H<sub>2</sub>-TPR and chemisorption, cobalt is clearly playing the role of a textural and electronic promoter, improving the reducibility and surface basicity of the catalyst. Based on the drawn correlation, the most significant factors, which are the closest to the sequence for activity of the tested catalysts, are basicity and hydrogen uptake of the materials. Both of those factors are

related to the improvement of adsorption of the reagents on the surface of the catalysts and support the dissociation of the reacting species on the active sites.

## 2.6 Post-run characterization

X-ray diffractograms for the spent catalysts are presented in Fig. 8. Spinel, periclase, and metallic nickel which were present in the reduced material were also detected in the post-reaction materials. Additionally, a residual phase of hydrotalcite was visible in all the materials. Hydrotalcites do present a memory effect, where in an environment rich in CO<sub>2</sub> and H<sub>2</sub>O, the layered structure may be partially rebuilt. Such conditions may be found in the methanation reaction, where gases rich in both carbon dioxide and water vapor flow through the catalytic bed, allowing the thermally decomposed hydrotalcites to partially rebuild their structure [38]. However, the intensity of the crystalline phase assigned to mixed oxides is much weaker in comparison to metallic nickel, than for the samples before the reaction. On the other hand, no scattering from the amorphous phase emerged in the diffractograms, which suggests high crystallinity of the samples, however, the presence of a small amount of amorphous phase cannot be definitely excluded. The reflections assigned to nickel are very sharp. The crystallite size presented in Fig. 8 is an average value of crystallite sizes calculated by the Scherrer equation for all significant nickel reflections at 44.44, 51.78, and 76.27 deg. Neither direct information on favoring sintering nor nickel redispersion was drawn by the addition of cobalt on Ni-hydrotalcite-derived catalysts. The Ni<sup>0</sup> crystallite size for the unpromoted catalyst increased after the methanation test. In the case of cobalt-promoted catalysts, an increase in crystallite size in post-run samples was detected for HTNi15Co1 and HTNi15Co4. The two-remaining cobalt-containing samples were found to have smaller Ni<sup>0</sup> particle sizes after the test than on reduced pre-run catalyst. However, the increase in particle size for the samples promoted with cobalt is smaller than for the unpromoted HTNi15. This suggests no obvious increase in sintering by promotion of nickel catalyst with small concentrations of cobalt.

Additionally, no crystalline carbon-related reflections were detected by XRD in the samples after reaction, proving that such type of carbonaceous species was not formed on the surface of the catalyst during the methanation test in quantity allowing for its identification with such method. Generally, coke formation is not a thermodynamically favored reaction in the temperature range of the methanation test (250–450°C) due to continuous hydrogenation of the carbon species formed at such temperatures [12].

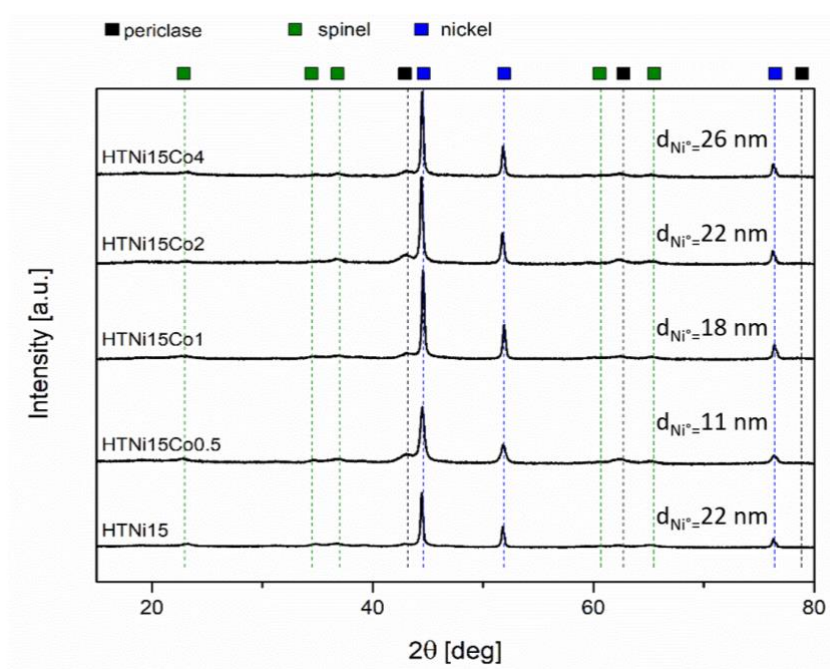


**Fig. 9.** Post-reaction X-ray diffractograms for hydrotalcite-derived catalysts

### 3. Conclusions

Cobalt-promoted hydrotalcite-derived catalyst is an interesting material for the CO<sub>2</sub> methanation reaction. Cobalt plays a role as a textural and electronic promoter, improving the surface properties such as acidic/basic properties and reducibility of nickel. Co-Ni synergy effect cannot be excluded although this work does not provide conclusive information on this subject, foremost due to low concentrations of cobalt in the active phase. The Ni-hydrotalcite sample promoted with 1 wt% cobalt, was the most active with 77% CO<sub>2</sub> conversion at 300 °C and near-equilibrium activity above that temperature. Moreover, all the cobalt-containing samples were very active and selective in the CO<sub>2</sub> methanation reaction. Cobalt promotion does not favor the sintering of nickel crystallites. The structure and activity of the catalyst remained stable during the 24 hours test at 300 °C. Despite the relatively large metallic nickel crystallites in the reduced Co-promoted catalysts, samples were maintaining the activity and selectivity for methanation, which is probably due to the dominating Ni<sup>0</sup> species at the surface of the catalysts as reported in XPS for HTNi15Co1. The most significant factor for the increased activity of the HTNi15Co1 sample was the number of basic sites – highest among the tested samples. It may be concluded that addition of cobalt in low amounts (0.5-1 wt%) is providing optimum improvement of the surface properties, such as basicity, hydrogen uptake and additionally is related to formation of relatively small Ni<sup>0</sup> crystallites on the surface, which resulted in catalytic material with satisfactory performance.

In comparison to other Ni-Co catalytic systems reported in the literature [24,26], certain properties such as good stability, increased activity, improved reducibility etc. were confirmed. It is hard to clearly compare which among the catalysts available in the literature and this study is the most optimal for the methanation reaction, due to the different loadings of Ni and Co used, however, many factors make Ni-Co catalysts promising material for the CO<sub>2</sub> methanation.

## Acknowledgments:

Paulina Summa would like to kindly acknowledge The French Embassy in Poland for providing the scholarship.

Bogdan Samojeden and Monika Motak would like to thank for their financial support grant AGH nr 16.16.210.476.

Katarzyna Świrk is MSCA-IF researcher at the Norwegian University of Science and Technology in Norway. This project has received funding from the European Union's Horizon 2020 research and innovation programme under the Marie Skłodowska-Curie grant agreement No 892571.

## References:

- [1] D. Lüthi, M. Le Floch, B. Bereiter, T. Blunier, J.M. Barnola, U. Siegenthaler, D. Raynaud, J. Jouzel, H. Fischer, K. Kawamura, T.F. Stocker, High-resolution carbon dioxide concentration record 650,000-800,000 years before present, *Nature*. 453 (2008) 379–382. <https://doi.org/10.1038/nature06949>.
- [2] R.J.H. Dunn, D.M. Stanitski, N. Gobron, K.M. Willett, Global climate, *Bull. Am. Meteorol. Soc.* 101 (2020) S9–S128. <https://doi.org/10.1175/BAMS-D-20-0104.1>.
- [3] CO2 Earth, Earth's CO2 Home Page, CO2 Earth. 2014 (2007). <https://www.co2.earth/> (accessed November 23, 2020).
- [4] Rebecca Lindsey, Climate Change: Atmospheric Carbon Dioxide, (2020). <https://www.climate.gov/news-features/understanding-climate/climate-change-atmospheric-carbon-dioxide#:~:text=The global average atmospheric carbon,least the past 800%2C000 years.> (accessed November 12, 2020).
- [5] G. Macdonald, H. Abarbanel, P. Carruthers, The long term impact of atmospheric carbon dioxide on climate., SRI International, 1979.
- [6] M. Aresta, Carbon dioxide utilization: Chemical, biological and technological applications, *Greenh. Gases Mitig. Util. CHEMRAWN-XVII ICCDU-IX Conf.* July 8 to 12, 2007. (2009) 123–149.
- [7] E. Alper, O. Yuksel Orhan, CO2 utilization: Developments in conversion processes, *Petroleum*. 3 (2017) 109–126. <https://doi.org/10.1016/j.petlm.2016.11.003>.
- [8] D. Wierzbicki, M. Motak, T. Grzybek, M.E. Gálvez, P. Da Costa, The influence of lanthanum incorporation method on the performance of nickel-containing hydrotalcite-derived catalysts in CO2 methanation reaction, *Catal. Today*. 307 (2018) 205–211. <https://doi.org/10.1016/j.cattod.2017.04.020>.
- [9] G. Garbarino, P. Riani, L. Magistri, G. Busca, A study of the methanation of carbon

- dioxide on Ni/Al<sub>2</sub>O<sub>3</sub> catalysts at atmospheric pressure, *Int. J. Hydrogen Energy*. 39 (2014) 11557–11565. <https://doi.org/10.1016/j.ijhydene.2014.05.111>.
- [10] S.E. Olesen, K.J. Andersson, C.D. Damsgaard, I. Chorkendorff, Deactivating Carbon Formation on a Ni/Al<sub>2</sub>O<sub>3</sub> Catalyst under Methanation Conditions, *J. Phys. Chem. C*. 121 (2017) 15556–15564. <https://doi.org/10.1021/acs.jpcc.7b03754>.
- [11] X. Bai, S. Wang, T. Sun, S. Wang, The sintering of Ni/Al<sub>2</sub>O<sub>3</sub> methanation catalyst for substitute natural gas production, *React. Kinet. Mech. Catal.* 112 (2014) 437–451. <https://doi.org/10.1007/s11144-014-0700-8>.
- [12] C. Mirodatos, H. Praliaud, M. Primet, Deactivation of nickel-based catalysts during CO methanation and disproportionation, *J. Catal.* 107 (1987) 275–287. [https://doi.org/10.1016/0021-9517\(87\)90294-6](https://doi.org/10.1016/0021-9517(87)90294-6).
- [13] C.H. Bartholomew, Mechanisms of catalyst deactivation, *Appl. Catal. A Gen.* 212 (2001) 17–60. [https://doi.org/10.1016/S0926-860X\(00\)00843-7](https://doi.org/10.1016/S0926-860X(00)00843-7).
- [14] P. Grange, *Catalysis Reviews : Science and Engineering Catalytic Hydrodesulfurization*, 21 (1980) 37–41.
- [15] M.A.A. Aziz, A.A. Jalil, S. Triwahyono, R.R. Mukti, Y.H. Taufiq-Yap, M.R. Sazegar, Highly active Ni-promoted mesostructured silica nanoparticles for CO<sub>2</sub> methanation, *Appl. Catal. B Environ.* 147 (2014) 359–368. <https://doi.org/10.1016/j.apcatb.2013.09.015>.
- [16] P. Frontera, A. Macario, M. Ferraro, P.L. Antonucci, Supported catalysts for CO<sub>2</sub> methanation: A review, *Catalysts*. 7 (2017) 1–28. <https://doi.org/10.3390/catal7020059>.
- [17] E.M. Köck, M. Kogler, T. Bielz, B. Klötzer, S. Penner, In situ FT-IR spectroscopic study of CO<sub>2</sub> and CO adsorption on Y<sub>2</sub>O<sub>3</sub>, ZrO<sub>2</sub>, and yttria-stabilized ZrO<sub>2</sub>, *J. Phys. Chem. C*. 117 (2013) 17666–17673. <https://doi.org/10.1021/jp405625x>.
- [18] S. Tada, T. Shimizu, H. Kameyama, T. Haneda, R. Kikuchi, Ni/CeO<sub>2</sub> catalysts with high CO<sub>2</sub> methanation activity and high CH<sub>4</sub> selectivity at low temperatures, *Int. J. Hydrogen Energy*. 37 (2012) 5527–5531. <https://doi.org/10.1016/j.ijhydene.2011.12.122>.
- [19] A. Cárdenas-Arenas, A. Quindimil, A. Davó-Quñonero, E. Bailón-García, D. Lozano-Castelló, U. De-La-Torre, B. Pereda-Ayo, J.A. González-Marcos, J.R. González-Velasco, A. Bueno-López, Design of active sites in Ni/CeO<sub>2</sub> catalysts for the methanation of CO<sub>2</sub>: tailoring the Ni-CeO<sub>2</sub> contact, *Appl. Mater. Today*. 19 (2020). <https://doi.org/10.1016/j.apmt.2020.100591>.
- [20] F. Ocampo, B. Louis, L. Kiwi-Minsker, A.C. Roger, Effect of Ce/Zr composition and noble metal promotion on nickel based CexZr1-xO2 catalysts for carbon dioxide methanation, *Appl. Catal. A Gen.* 392 (2011) 36–44. <https://doi.org/10.1016/j.apcata.2010.10.025>.
- [21] A.C. Bouali, M. Serdechnova, C. Blawert, J. Tedim, M.G.S. Ferreira, M.L. Zheludkevich, Layered double hydroxides (LDHs) as functional materials for the corrosion protection of aluminum alloys: A review, *Appl. Mater. Today*. 21 (2020) 100857. <https://doi.org/10.1016/j.apmt.2020.100857>.
- [22] D. Wierzbicki, R. Baran, R. Dębek, M. Motak, T. Grzybek, M.E. Gálvez, P. Da Costa, The influence of nickel content on the performance of hydrotalcite-derived catalysts in

- CO<sub>2</sub> methanation reaction, *Int. J. Hydrogen Energy*. (2017).  
<https://doi.org/10.1016/j.ijhydene.2017.02.148>.
- [23] F. Cavani, F. Trifiro, A. Vaccari, Hydrotalcite-type anionic clays: preparation, properties and applications, *II (1991)* 173-301 Elsevier Science Publishers, Catal. Today. 11 (1991) 173–301. <http://dns2.asia.edu.tw/~ysho/YSHO-English/2000Engineering/PDF/CatTod11,173.pdf>.
- [24] B. Alrafei, I. Polaert, A. Ledoux, F. Azzolina-Jury, Remarkably stable and efficient Ni and Ni-Co catalysts for CO<sub>2</sub> methanation, *Catal. Today*. (2020).  
<https://doi.org/10.1016/j.cattod.2019.03.026>.
- [25] L. Xu, X. Lian, M. Chen, Y. Cui, F. Wang, W. Li, B. Huang, CO<sub>2</sub> methanation over Co–Ni bimetal-doped ordered mesoporous Al<sub>2</sub>O<sub>3</sub> catalysts with enhanced low-temperature activities, *Int. J. Hydrogen Energy*. 43 (2018) 17172–17184.  
<https://doi.org/10.1016/j.ijhydene.2018.07.106>.
- [26] Q. Liu, B. Bian, J. Fan, J. Yang, Cobalt doped Ni based ordered mesoporous catalysts for CO<sub>2</sub> methanation with enhanced catalytic performance, *Int. J. Hydrogen Energy*. (2018). <https://doi.org/10.1016/j.ijhydene.2018.01.132>.
- [27] P. Shafiee, S.M. Alavi, M. Rezaei, Solid-state synthesis method for the preparation of cobalt doped Ni–Al<sub>2</sub>O<sub>3</sub> mesoporous catalysts for CO<sub>2</sub> methanation, *Int. J. Hydrogen Energy*. (2020). <https://doi.org/10.1016/j.ijhydene.2020.10.221>.
- [28] Y. Varun, I. Sreedhar, S.A. Singh, Highly stable M/NiO–MgO (M = Co, Cu and Fe) catalysts towards CO<sub>2</sub> methanation, *Int. J. Hydrogen Energy*. (2020).  
<https://doi.org/10.1016/j.ijhydene.2020.07.212>.
- [29] D. Li, S. Xu, K. Song, C. Chen, Y. Zhan, L. Jiang, Hydrotalcite-derived Co/Mg(Al)O as a stable and coke-resistant catalyst for low-temperature carbon dioxide reforming of methane, *Appl. Catal. A Gen.* 552 (2018) 21–29.  
<https://doi.org/10.1016/j.apcata.2017.12.022>.
- [30] A.F. Lucrédio, E.M. Assaf, Cobalt catalysts prepared from hydrotalcite precursors and tested in methane steam reforming, *J. Power Sources*. 159 (2006) 667–672.  
<https://doi.org/10.1016/j.jpowsour.2005.10.108>.
- [31] G. Busca, U. Costantino, T. Montanari, G. Ramis, C. Resini, M. Sisani, Nickel versus cobalt catalysts for hydrogen production by ethanol steam reforming: Ni-Co-Zn-Al catalysts from hydrotalcite-like precursors, *Int. J. Hydrogen Energy*. 35 (2010) 5356–5366. <https://doi.org/10.1016/j.ijhydene.2010.02.124>.
- [32] G. De Souza, V.C. Ávila, N.R. Marcílio, O.W. Perez-Lopez, Synthesis gas production by steam reforming of ethanol over M-Ni-Al hydrotalcite-type catalysts; M = Mg, Zn, Mo, Co, *Procedia Eng.* 42 (2012) 1805–1815.  
<https://doi.org/10.1016/j.proeng.2012.07.575>.
- [33] A.D. Shejale, G.D. Yadav, Cu promoted Ni-Co/hydrotalcite catalyst for improved hydrogen production in comparison with several modified Ni-based catalysts via steam reforming of ethanol, *Int. J. Hydrogen Energy*. 42 (2017) 11321–11332.  
<https://doi.org/10.1016/j.ijhydene.2017.03.052>.
- [34] R. Guil-López, R.M. Navarro, M.A. Peña, J.L.G. Fierro, Hydrogen production by oxidative ethanol reforming on Co, Ni and Cu ex-hydrotalcite catalysts, *Int. J.*

- Hydrogen Energy. 36 (2011) 1512–1523.  
<https://doi.org/10.1016/j.ijhydene.2010.10.084>.
- [35] H. Long, Y. Xu, X. Zhang, S. Hu, S. Shang, Y. Yin, X. Dai, Ni-Co/Mg-Al catalyst derived from hydrotalcite-like compound prepared by plasma for dry reforming of methane, *J. Energy Chem.* 22 (2013) 733–739. [https://doi.org/10.1016/S2095-4956\(13\)60097-2](https://doi.org/10.1016/S2095-4956(13)60097-2).
- [36] C. Tanios, S. Bsaibes, C. Gennequin, M. Labaki, F. Cazier, S. Billet, H.L. Tidahy, B. Nsouli, A. Aboukaïs, E. Abi-Aad, Syngas production by the CO<sub>2</sub> reforming of CH<sub>4</sub> over Ni–Co–Mg–Al catalysts obtained from hydrotalcite precursors, *Int. J. Hydrogen Energy.* 42 (2017) 12818–12828. <https://doi.org/10.1016/j.ijhydene.2017.01.120>.
- [37] R. Zavoianu, R. Ionescu, O.D. Pavel, R. Bîrjega, E. Angelescu, Comparison between MeII/Mg/Al hydrotalcites and hydrotalcite-supported Me(II) acetylacetonates (Me(II)=Co, Cu or Ni) catalysts for the epoxidation of cyclohexene with molecular oxygen, *Appl. Clay Sci.* 52 (2011) 1–10. <https://doi.org/10.1016/j.clay.2011.01.014>.
- [38] Z. Xia, L. Qin, W. Zhou, H. Wang, B. Yu, Z. Sun, J. Qian, M. He, An efficient aerobic oxidative phosphonation of  $\alpha$ -amino C–H bonds over CoNiFe hydrotalcite, *Tetrahedron Lett.* 60 (2019) 151121. <https://doi.org/10.1016/j.tetlet.2019.151121>.
- [39] P. Liu, K. You, R. Deng, Z. Chen, J. Jian, F. Zhao, P. Liu, Q. Ai, H. Luo, Hydrotalcite-derived Co-MgAlO mixed metal oxides as efficient and stable catalyst for the solvent-free selective oxidation of cyclohexane with molecular oxygen, *Mol. Catal.* 466 (2019) 130–137. <https://doi.org/10.1016/j.mcat.2019.01.019>.
- [40] J. Liu, K. Wu, Z. Li, W. Li, Y. Ning, W. Wang, Y. Yang, Preparation of bimetal Co–Ni supported on Mg–Al oxide for chemocatalytic upgrading of tailored fermentation products to energy intensive fuels, *Green Energy Environ.* (2020). <https://doi.org/10.1016/j.gee.2020.10.011>.
- [41] J. Estephane, S. Aouad, S. Hany, B. El Khoury, C. Gennequin, H. El Zakhem, J. El Nakat, A. Aboukaïs, E. Abi Aad, CO<sub>2</sub> reforming of methane over Ni-Co/ZSM5 catalysts. Aging and carbon deposition study, *Int. J. Hydrogen Energy.* 40 (2015) 9201–9208. <https://doi.org/10.1016/j.ijhydene.2015.05.147>.
- [42] H. Insight, E.S. Zhitova, H.C. Greenwell, M.G. Krzhizhanovskaya, D.C. Apperley, I. V. Pekov, V.N. Yakovenchuk, Thermal Evolution of Natural Layered Double and Cl-Members of the Hydrotalcite Supergroup, (n.d.).
- [43] H.P. Klug, L.E. Alexander, *X-Ray Diffraction Procedures: For Polycrystalline and Amorphous Materials*, 2nd Edition, 1974.
- [44] L. He, H. Berntsen, E. Ochoa-Fernández, J.C. Walmsley, E.A. Blekkan, D. Chen, Co-Ni catalysts derived from hydrotalcite-like materials for hydrogen production by ethanol steam reforming, *Top. Catal.* 52 (2009) 206–217. <https://doi.org/10.1007/s11244-008-9157-1>.
- [45] H. Xin, K. Guo, D. Li, H. Yang, C. Hu, Production of high-grade diesel from palmitic acid over activated carbon-supported nickel phosphide catalysts, *Appl. Catal. B Environ.* 187 (2016) 375–385. <https://doi.org/10.1016/j.apcatb.2016.01.051>.
- [46] J.A. Dumesic, G.W. Huber, M. Boudart, *Principles of Heterogeneous Catalysis*, in: *Handb. Heterog. Catal.*, American Cancer Society, 2008.

<https://doi.org/https://doi.org/10.1002/9783527610044.hetcat0001>.

- [47] G. Kumar, H. Bossert, D. McDonald, A. Chatzidimitriou, M.A. Ardagh, Y. Pang, C.S. Lee, M. Tsapatsis, O.A. Abdelrahman, P.J. Dauenhauer, Catalysis-in-a-Box: Robotic Screening of Catalytic Materials in the Time of COVID-19 and Beyond, *Matter*. 3 (2020) 805–823. <https://doi.org/10.1016/j.matt.2020.06.025>.
- [48] S. and B.M. Dumesic, J. A., Topsoe, H Khammouma, Surface, Catalytic and Magnetic Properties of Small Iron Particles, *J. Catal.* 37 (1975) 503–512.
- [49] G. Ertl, H. Knözinger, J. Weitkamp, Handbook of Heterogeneous Catalysis, *Handb. Heterog. Catal.* 1–5 (2008) 1–2497. [https://doi.org/10.1524/zpch.1999.208.part\\_1\\_2.274](https://doi.org/10.1524/zpch.1999.208.part_1_2.274).
- [50] V. Rives, Characterisation of layered double hydroxides and their decomposition products, *Mater. Chem. Phys.* 75 (2002) 19–25. [https://doi.org/10.1016/S0254-0584\(02\)00024-X](https://doi.org/10.1016/S0254-0584(02)00024-X).
- [51] X. Yu, F. Zhang, W. Chu, Effect of a second metal (Co, Cu, Mn or Zr) on nickel catalysts derived from hydrotalcites for the carbon dioxide reforming of methane, *RSC Adv.* 6 (2016) 70537–70546. <https://doi.org/10.1039/c6ra12335j>.
- [52] R. Dębek, M. Motak, D. Duraczyska, F. Launay, M.E. Galvez, T. Grzybek, P. Da Costa, Methane dry reforming over hydrotalcite-derived Ni-Mg-Al mixed oxides: The influence of Ni content on catalytic activity, selectivity and stability, *Catal. Sci. Technol.* 6 (2016) 6705–6715. <https://doi.org/10.1039/c6cy00906a>.
- [53] K. Świrk, P. Summa, D. Wierzbicki, M. Motak, P. Da Costa, Vanadium promoted Ni(Mg,Al)O hydrotalcite-derived catalysts for CO<sub>2</sub> methanation, *Int. J. Hydrogen Energy.* (2021). <https://doi.org/10.1016/j.ijhydene.2021.02.172>.
- [54] C. Liang, H. Tian, G. Gao, S. Zhang, Q. Liu, D. Dong, X. Hu, Methanation of CO<sub>2</sub> over alumina supported nickel or cobalt catalysts: Effects of the coordination between metal and support on formation of the reaction intermediates, *Int. J. Hydrogen Energy.* 45 (2020) 531–543. <https://doi.org/10.1016/j.ijhydene.2019.10.195>.
- [55] Z. Qin, X. Wang, L. Dong, T. Su, B. Li, Y. Zhou, Y. Jiang, X. Luo, H. Ji, CO<sub>2</sub> methanation on Co/TiO<sub>2</sub> catalyst: Effects of Y on the support, *Chem. Eng. Sci.* (2019). <https://doi.org/10.1016/j.ces.2019.115245>.
- [56] Y. Yu, S. Mottaghi-Tabar, M.W. Iqbal, A. Yu, D.S.A. Simakov, CO<sub>2</sub> methanation over alumina-supported cobalt oxide and carbide synthesized by reverse microemulsion method, *Catal. Today.* (2020). <https://doi.org/10.1016/j.cattod.2020.08.017>.
- [57] O.J. Olusola, M. Sudip, Temperature programme reduction (TPR) studies of cobalt phases in -alumina supported cobalt catalysts, *J. Pet. Technol. Altern. Fuels.* 7 (2016) 1–12. <https://doi.org/10.5897/jptaf2015.0122>.
- [58] T.A. Le, M.S. Kim, S.H. Lee, E.D. Park, CO and CO<sub>2</sub> Methanation Over Supported Cobalt Catalysts, *Top. Catal.* 60 (2017) 714–720. <https://doi.org/10.1007/s11244-017-0788-y>.
- [59] Z.A. Allothman, A review: Fundamental aspects of silicate mesoporous materials, *Materials (Basel).* 5 (2012) 2874–2902. <https://doi.org/10.3390/ma5122874>.
- [60] D. Wierzbicki, M.V. Moreno, S. Ognier, M. Motak, T. Grzybek, P. Da Costa, M.E.

- Gálvez, Ni-Fe layered double hydroxide derived catalysts for non-plasma and DBD plasma-assisted CO<sub>2</sub> methanation, *Int. J. Hydrogen Energy*. 45 (2020) 10423–10432. <https://doi.org/10.1016/j.ijhydene.2019.06.095>.
- [61] J. Niu, S.E. Liland, J. Yang, K.R. Rout, J. Ran, D. Chen, Effect of oxide additives on the hydrotalcite derived Ni catalysts for CO<sub>2</sub> reforming of methane, *Chem. Eng. J.* 377 (2019) 0–1. <https://doi.org/10.1016/j.cej.2018.08.149>.
- [62] W.Y. Hernández, F. Aliç, A. Verberckmoes, P. Van Der Voort, Tuning the acidic–basic properties by Zn-substitution in Mg–Al hydrotalcites as optimal catalysts for the aldol condensation reaction, *J. Mater. Sci.* 52 (2017) 628–642. <https://doi.org/10.1007/s10853-016-0360-3>.
- [63] P. Summa, B. Samojeden, M. Motak, D. Wierzbicki, I. Alxneit, K. Świerczek, P. Da Costa, Investigation of Cu promotion effect on hydrotalcite-based nickel catalyst for CO<sub>2</sub> methanation, *Catal. Today*. (2021). <https://doi.org/https://doi.org/10.1016/j.cattod.2021.05.004>.
- [64] P.T. Andrews, T. Collins, P. Weightman, The influence of the number of unoccupied 3d states on the L 3M<sub>4,5</sub>M<sub>4,5</sub> Auger spectrum of Ni, *J. Phys. C Solid State Phys.* 14 (1981) 4–8. <https://doi.org/10.1088/0022-3719/14/31/006>.
- [65] G. Ertl, R. Hierl, H. Knözinger, N. Thiele, H.P. Urbach, XPS study of copper aluminate catalysts, *Appl. Surf. Sci.* 5 (1980) 49–64. [https://doi.org/10.1016/0378-5963\(80\)90117-8](https://doi.org/10.1016/0378-5963(80)90117-8).
- [66] M.G.E. Wagner C.D., Riggs W.M., Davis L.E., Moulder J.F., *Handbook of X-Ray Photoelectron Spectroscopy*, 1979.
- [67] E.S. Lambers, C.N. Dykstal, J.M. Seo, J.E. Rowe, P.H. Holloway, Room-temperature oxidation of Ni(110) at low and atmospheric oxygen pressures, *Oxid. Met.* 45 (1996) 301–321. <https://doi.org/10.1007/BF01046987>.
- [68] N.H. Turner, A.M. Single, Determination of peak positions and areas from wide-scan XPS spectra, *Surf. Interface Anal.* 15 (1990) 215–222. <https://doi.org/10.1002/sia.740150305>.
- [69] L. Gao, E. Han, Y. He, C. Du, J. Liu, X. Yang, Effect of different templating agents on cobalt ferrite (CoFe<sub>2</sub>O<sub>4</sub>) nanomaterials for high-performance supercapacitor, *Ionics (Kiel)*. 26 (2020) 3643–3654. <https://doi.org/10.1007/s11581-020-03482-z>.
- [70] B.J. Tan, K.J. Klabunde, P.M.A. Sherwood, XPS Studies of Solvated Metal Atom Dispersed Catalysts. Evidence for Layered Cobalt–Manganese Particles on Alumina and Silica, *J. Am. Chem. Soc.* 113 (1991) 855–861. <https://doi.org/10.1021/ja00003a019>.
- [71] C.E. Dubé, B. Workie, S.P. Kounaves, A. Robbat, M.L. Aksub, G. Davies, Electrodeposition of Metal Alloy and Mixed Oxide Films Using a Single-Precursor Tetranuclear Copper-Nickel Complex, *J. Electrochem. Soc.* 142 (1995) 3357–3365. <https://doi.org/10.1149/1.2049987>.
- [72] S.C. Petitto, E.M. Marsh, G.A. Carson, M.A. Langell, Cobalt oxide surface chemistry: The interaction of CoO(1 0 0), Co<sub>3</sub>O<sub>4</sub>(1 1 0) and Co<sub>3</sub>O<sub>4</sub>(1 1 1) with oxygen and water, *J. Mol. Catal. A Chem.* 281 (2008) 49–58. <https://doi.org/10.1016/j.molcata.2007.08.023>.

- [73] S. Fan, X. Li, M. Qin, J. Mu, L. Wang, G. Gan, X. Wang, A. Chen, Rational Design of Peroxymonosulfate Activation and Photoinduced Catalysis Tandem Systems for Artificial Conversion of Solar Light to Chemical Energy, *ACS Omega*. 4 (2019) 4113–4128. <https://doi.org/10.1021/acsomega.8b03071>.
- [74] J.T. Richardson, T.S. Cale, Interpretation of hydrogen chemisorption on nickel catalysts, *J. Catal.* 102 (1986) 419–432. [https://doi.org/10.1016/0021-9517\(86\)90177-6](https://doi.org/10.1016/0021-9517(86)90177-6).
- [75] R.J. Liu, P.A. Crozier, C.M. Smith, D.A. Hucul, J. Blackson, G. Salaita, Metal sintering mechanisms and regeneration of palladium/alumina hydrogenation catalysts, *Appl. Catal. A Gen.* 282 (2005) 111–121. <https://doi.org/10.1016/j.apcata.2004.12.015>.
- [76] S. Sengupta, K. Ray, G. Deo, Effects of modifying Ni/Al<sub>2</sub>O<sub>3</sub> catalyst with cobalt on the reforming of CH<sub>4</sub> with CO<sub>2</sub> and cracking of CH<sub>4</sub> reactions, *Int. J. Hydrogen Energy*. 39 (2014) 11462–11472. <https://doi.org/10.1016/j.ijhydene.2014.05.058>.
- [77] M. Boudart, Turnover Rates in Heterogeneous Catalysis, *Chem. Rev.* 95 (1995) 661–666. <https://doi.org/10.1021/cr00035a009>.
- [78] J.A. Martins, A.C. Faria, M.A. Soria, C. V. Miguel, A.E. Rodrigues, L.M. Madeira, CO<sub>2</sub> methanation over hydrotalcite-derived nickel/ruthenium and supported ruthenium catalysts, *Catalysts*. 9 (2019) 1008. <https://doi.org/10.3390/catal9121008>.
- [79] C. Sun, K. Świrk, D. Wierzbicki, M. Motak, T. Grzybek, P. Da Costa, On the effect of yttrium promotion on Ni-layered double hydroxides-derived catalysts for hydrogenation of CO<sub>2</sub> to methane, *Int. J. Hydrogen Energy*. (2020). <https://doi.org/10.1016/j.ijhydene.2020.03.202>.